




Article

Fundamental Material Properties of the 2LiBH₄-MgH₂ Reactive Hydride Composite for Hydrogen Storage: (II) Kinetic Properties

Julian Jepsen ^{1,*} , Chiara Milanese ² , Julián Puszkiet ^{1,3}, Alessandro Girella ², Benedetto Schiavo ⁴, Gustavo A. Lozano ^{1,†}, Giovanni Capurso ¹ , José M. Bellosta von Colbe ¹, Amedeo Marini ³, Stephan Kabelac ⁵, Martin Dornheim ¹ and Thomas Klassen ¹

¹ Institute of Materials Research, Helmholtz-Zentrum Geesthacht, Max-Planck-Straße 1, 21502 Geesthacht, Germany; julian.puszkiet@hzg.de (J.P.); gusaloz@yahoo.com (G.A.L.); Giovanni.Capurso@hzg.de (G.C.); jose.bellostavoncolbe@hzg.de (J.M.B.v.C.); martin.dornheim@hzg.de (M.D.); thomas.klassen@hzg.de (T.K.)

² Pavia H2 Lab, Department of Chemistry, Physical Chemistry Division, University of Pavia, Viale Taramelli 16, 27100 Pavia, Italy; chiara.milanese@unipv.it (C.M.); buondi.giro@gmail.com (A.G.)

³ Department of Physicochemistry of Materials, Consejo Nacional de Investigaciones Científicas y Técnicas (CONICET), Centro Atómico Bariloche, Av. Bustillo km 9500, R8402AGP S.C. de Bariloche, Argentina; amedeo.marini@unipv.it

⁴ Dipartimento dell'Innovazione Industriale e Digitale (DIID)-Ingegneria Chimica Gestionale Informatica Meccanica, Università degli Studi di Palermo, viale delle Scienze, Ed. 6, 90128 Palermo, Italy, and Istituto per le Tecnologie Avanzate (ITA), SS 113 174, 91100 Trapani, Italy; bennyschiavo@gmail.com

⁵ Institute for Thermodynamics, Leibniz Universität Hannover, Callinstraße 36, 30167 Hannover, Germany; kabelac@ifw.uni-hannover.de

* Correspondence: julian.jepsen@hzg.de; Tel.: +49-4152-87-2602; Fax: +49-4152-87-2625

† Current Address: BASF SE, Carl Bosch Str 38, 67056 Ludwigshafen, Germany.

Received: 4 April 2018; Accepted: 27 April 2018; Published: 7 May 2018



Abstract: Reaction kinetic behaviour and cycling stability of the 2LiBH₄-MgH₂ reactive hydride composite (Li-RHC) are experimentally determined and analysed as a basis for the design and development of hydrogen storage tanks. In addition to the determination and discussion about the properties; different measurement methods are applied and compared. The activation energies for both hydrogenation and dehydrogenation are determined by the Kissinger method and via the fitting of solid-state reaction kinetic models to isothermal volumetric measurements. Furthermore, the hydrogen absorption–desorption cycling stability is assessed by titration measurements. Finally, the kinetic behaviour and the reversible hydrogen storage capacity of the Li-RHC are discussed.

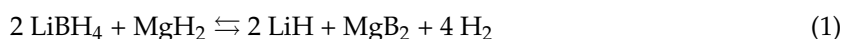
Keywords: hydrogen storage; LiBH₄-MgH₂; metal hydrides; borohydrides; reactive hydride composites; material properties

1. Introduction

Hydrogen technologies, including the hydrogen generation from renewable energy sources, its storage by physical or chemical means, as well as the reconversion to energy using fuel cells, have been considered for a long time as a possible energy scenario for the future. On the one hand, the hydrogen storage is particularly interesting, because hydrogen offers a high gravimetric energy density value (33.33 kWh·kg⁻¹) already at ambient pressure and temperature [1]. On the other hand, this diatomic gas displays also a very low density (0.08988 kg·m⁻³), which results in a less appealing value for the volumetric energy density (2.99 kWh·m⁻³) [2]. Thus, it is important to improve the value of the volumetric energy density without significantly reducing the gravimetric density. This is

needed to be competitive with other widely-used energy vectors, such as compressed natural gas ($\sim 13.9 \text{ kWh}\cdot\text{kg}^{-1}/\sim 2700 \text{ kWh}\cdot\text{m}^{-3}$) and gasoline ($\sim 12.2 \text{ kWh}\cdot\text{kg}^{-1}/\sim 8700 \text{ kWh}\cdot\text{m}^{-3}$), or even other energy storage systems, like lithium-ion batteries ($\sim 0.2 \text{ kWh}\cdot\text{kg}^{-1}/\sim 500 \text{ kWh}\cdot\text{m}^{-3}$) [3]. The storage method itself can improve this value drastically. By means of physical storage, hydrogen is either compressed up to 700 bar, or liquefied at $-253 \text{ }^\circ\text{C}$. These storage techniques, and in particular, the vessel structures and the gas processing, are relatively complex and energy demanding. Hence, both techniques are not the most suitable from an economic perspective [4]. Complex and intermetallic hydrides offer the possibility to increase the volumetric density of hydrogen considerably, for instance, LiBH_4 possesses a volumetric density of $121 \text{ kg H}_2 \text{ m}^{-3}$ [5] and Mg_2FeH_6 has the highest known volumetric density of $150 \text{ kg H}_2 \text{ m}^{-3}$ [6]. In such metal hydrides, the chemical bonds with the metal atoms/ions allow interatomic distances, which are much shorter than in the molecular state of hydrogen, where repulsive forces are present. Metal hydrides, such as magnesium hydride (MgH_2), have been studied for hydrogen storage over several decades [7]. However, their practical applications, especially the mobile ones, are precluded either by their high thermodynamic stability or by slow reaction kinetic behaviour inter alia, due to high activation energies. These activation energies are controlled, among other influences, by different rate-limiting steps, such as the molecular dissociation of the diatomic hydrogen on the material surface, low diffusion rates of the reactants and/or insufficient nucleation [8–11]. Considerable advancements have been achieved with the use of additives and catalysts (e.g., [12,13]), and the application of appropriate processing techniques, such as mechanical milling (e.g., [14,15]).

Due to some of the properties of MgH_2 , such as a gravimetric hydrogen storage capacity of 7.6 wt % and material cost, this hydride is considered as one of the most promising materials for solid-state hydrogen storage. Nevertheless, its high thermodynamic stability ($73 \pm 2 \text{ kJ mol}^{-1} \text{ H}_2$ [16,17]) limits the practical use of the Mg/MgH_2 system [18,19]. One of the approaches, used to reduce the stability of hydrides, is through the combination of a binary hydride—such as MgH_2 —with light-metal complex hydrides, as for example, LiBH_4 . This approach, known as “reactive hydride composites” (RHC) [20,21], lowers the overall reaction enthalpy, owing to the exothermal formation of a compound upon endothermal dehydrogenation. Lithium borohydride (LiBH_4) is, hereby, a complex hydride of special interest, as it is among the materials with the highest theoretical gravimetric hydrogen storage density (18.5 wt % [22,23]). The combination of LiBH_4 with MgH_2 in a RHC (hereafter labelled Li-RHC) reduces the theoretical thermodynamic stability to $46 \text{ kJ mol}^{-1} \text{ H}_2$, according to Equation (1) [2]:



Apart from the abovementioned reduced thermodynamic stability, the Li-RHC presents several other advantages, among which the high theoretical gravimetric hydrogen storage capacity of 11.54 wt % and the considerable potential for further cost reduction in a hydrogen storage system [4].

This is the second study in a two-part investigation based on a more comprehensive analysis on the technical and economic evaluation of the system [24]. In the first study, the thermodynamic and heat transfer properties have been described [16], while in this study, the kinetic properties are analysed. Based on these properties, further advances in the optimisation via numerical simulation can be performed, to contribute towards the design of novel hydrogen storage systems based on the RHC concept.

2. Experimental Details

2.1. Sample Preparation

The elements in the desorbed state of the RHC (i.e., the right side of Equation (1)) were chosen as starting components in a molar ratio of $2\text{LiH}:1\text{MgB}_2$, adding 0.05 mol of titanium trichloride (TiCl_3) to enhance the kinetic behaviour. Lithium hydride powder (LiH , $\geq 99.4\%$ purity) and magnesium boride powder (MgB_2 , $\sim 99.4\%$ purity) were purchased from Alfa Aesar (Tewksbury, MA, USA), TiCl_3 powder

($\geq 99.995\%$ purity) from Sigma Aldrich (St. Louis, MO, USA). The materials were mixed and processed in a planetary ball mill (Pulverisette 5, Fritsch, Idar-Oberstein, Germany) at 230 rpm, with a ball to powder ratio of 10:1 for 20 h. After the milling operations, the composite was compacted with a load of 0.1 ton in a die with 5 mm diameter, resulting in a compaction pressure of 50 MPa, by using a uniaxial hydraulic press (Specac, Manual Hydraulic Press, Orpington, UK) [25]. All handling of the samples was carried out under inert gas atmosphere within a glove box filled with continuously purified Argon (~ 10 ppm of O_2 and H_2O).

2.2. Experimental Methods

2.2.1. Differential Scanning Calorimetry

A Sensys high-pressure differential scanning calorimeter (HP-DSC—Setaram, Caluire, Lyon, France) was used for the activation energy determination. The measurements were performed with H_2 pressures of 30 bar and 50 bar for absorption, and 3 bar for desorption by heating about 40 mg of sample at different heating rates of 0.5, 2, 5, and $10\text{ }^\circ\text{C}\cdot\text{min}^{-1}$. Before performing the measurements with the HP-DSC, the samples used to determine the activation energy underwent an activation process in the manometric instrument described in the following. The conditions for this single activation step were $350\text{ }^\circ\text{C}$ and 50 bar for absorption, and $400\text{ }^\circ\text{C}$ and 3 bar of H_2 for desorption.

2.2.2. Kinetic Studies

The hydrogenation rates and gravimetric capacities were assessed using a Sieverts apparatus (HERA Hydrogen Storage Systems, Longueil, QC, Canada) based on the differential pressure technique, and also, with another manometric apparatus (PCTPro 2000, Setaram, Caluire, Lyon, France) based on the absolute pressure technique. The hydrogen gas used in the experiments had a purity of 99.999% ($5.0\text{ }H_2$). The temperature and pressure conditions are provided for each experiment in the text. The mass of sample for all the measurements was approximately 150 mg. Additionally, a sample with a larger amount of material (500 mg) was evaluated.

2.2.3. Crystalline Phase Detection: X-ray Diffraction (XRD)

XRD analyses of the material after milling and hydrogenation/dehydrogenation cycling were performed using a Siemens D5000 X-ray diffractometer (Siemens, Munich, Germany) with $Cu\text{ }K\alpha$ radiation ($\lambda_{XRD} = 1.5406\text{ \AA}$) and in Bragg–Brentano geometry. In order to prevent the oxidation and hydrolysis of the sample, a plastic airtight X-ray transparent sample holder under Ar atmosphere was used.

2.2.4. Phase Equilibrium Compositions: Thermodynamic Calculations

To determine the nature of the Ti containing phases, thermodynamic calculations have been carried out using the HSC Chemistry software 9.4.1 [26]. The calculations have been performed based on the reactivity of the $2LiH + MgB_2$ with $TiCl_3$ under different temperature and pressure conditions. The most favourable reactions have been identified through a combination of Gibbs minimization equilibrium with selected solid and gas species. The obtained results represent ideal phase equilibrium compositions useful to predict possible reaction mechanisms between the Li-RHC matrix and the additive involving solid products and gaseous species such as B_2H_6 , B_xH_y ($x = 5$ to 12 , $y = 5$ to 14) and chlorine species. For all the calculations, the solid orthorhombic $LiBH_4$ (Pnma) is taken into account. $Li_2B_{12}H_{12}$ was not considered owing to the lack of available physicochemical data.

3. Results

3.1. Kinetic Properties

3.1.1. Activation Energy

The activation energy value has been calculated applying two different experimental methods. First, the activation energy has been measured via the Kissinger method [27], using the HP-DSC device. The activation energy E_a is calculated according to the equation [27]:

$$\frac{d \ln\left(\frac{\beta}{T_{\max}^2}\right)}{d\left(\frac{1}{T_{\max}}\right)} = -\frac{E_a}{R} \quad (2)$$

where β represents the heating rate for the curve and T_{\max} is the temperature at which the calorimetric peak is centred. The activation energy value can be calculated as the slope of the linear fit for the data acquired, plotting $\ln(\beta/T_{\max}^2)$ against $1000/T$, as suggested by Equation (2). In Figure 1a, the heat flow signal for the measurement under 50 bar of H_2 is plotted against temperature. In Figure 1b, the corresponding Kissinger plot is shown. The equivalent Kissinger plot for the measurement under 30 bar of hydrogen is also illustrated in Figure 1b. Taking into account the slopes displayed in Figure 1b, the activation energy values are calculated as $104 \pm 2 \text{ kJ mol}^{-1} H_2$ at 50 bar and $160 \pm 20 \text{ kJ mol}^{-1} H_2$ at 30 bar of applied H_2 pressure.

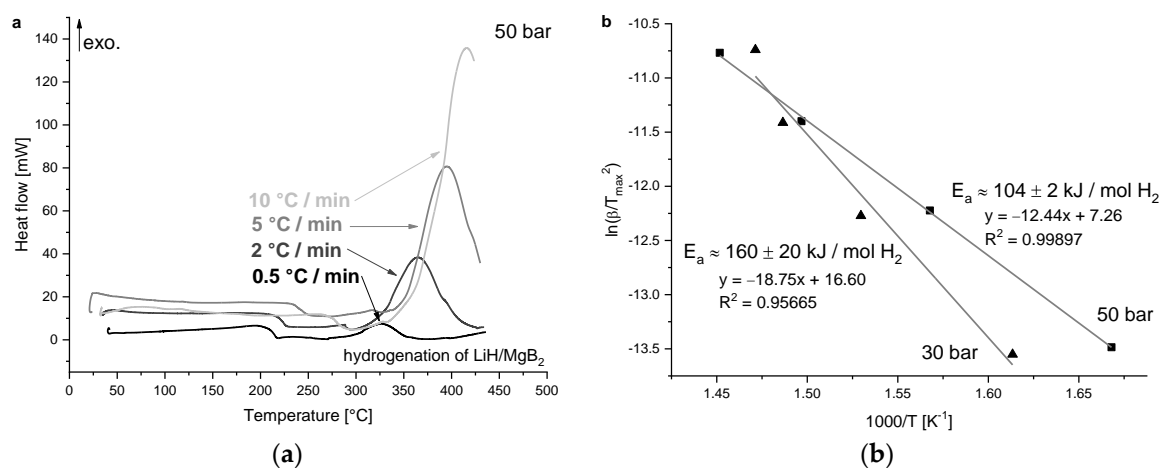


Figure 1. (a) Heat flow signal plotted vs temperature for four different heating rates at 50 bar of H_2 (absorption conditions) for the hydrogenation of LiH/MgB_2 ; (b) The resultant Kissinger plot as well as the Kissinger plot for the hydrogenation at 30 bar.

The measurements performed under desorption conditions, at 3 bar of H_2 , are shown in Figure 2. As it was already observed and discussed for the desorption Pressure Concentration Isotherms (PCI) curves in the previous study of this two-part investigation [16], in dynamic conditions, it is possible to observe two decomposition steps, in agreement with previously reported works [28,29]. Starting from these two distinct dehydrogenation processes, represented in Figure 2a by peak III and peak IV for MgH_2 and $LiBH_4$, respectively, the activation energy values can be calculated, as shown in Figure 2b.

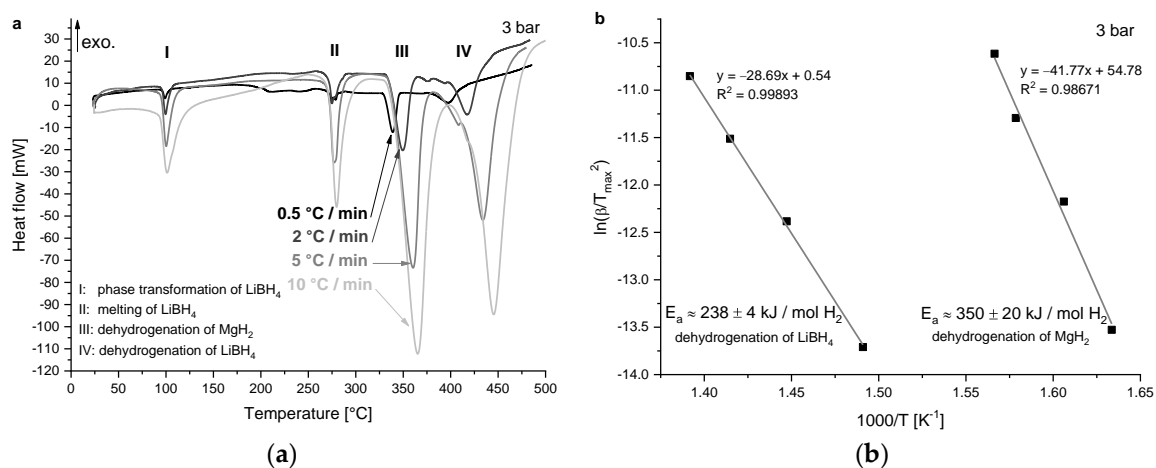


Figure 2. (a) Heat flow signal plotted vs temperature for four different heating rates at 3 bar of H_2 (desorption conditions) for the dehydrogenation of MgH_2 and $LiBH_4$; (b) The resultant Kissinger plots.

The calculated values for the activation energies result in $350 \pm 20 \text{ kJ mol}^{-1} H_2$ and $238 \pm 4 \text{ kJ mol}^{-1} H_2$ for the dehydrogenation process of MgH_2 and $LiBH_4$, respectively. The two calorimetric events, represented by peaks I and II in Figure 2a, and observed in the combined measurement in the previous study as well [16], are phase transformation steps, and have been already described in detail by other authors [28,30,31].

The activation energy values can be calculated applying a different technique and then compared with the previously obtained results. This second method consists in finding the reaction rate constant for several sorption measurements acquired by manometric analyses at different temperatures (Figure 3a). Both these methods are described in greater detail in a work by Varin et al. [3]. The reaction rate constant (labelled k) is a function of temperature, and expresses the evolution of the transformed fraction over time, being multiplied by the reaction model function [32]:

$$\frac{d\alpha}{dt} = k(T) \cdot f(\alpha) \quad (3)$$

The reaction model function $f(\alpha)$ is a function of the transformed fraction α , which is defined as fraction of hydrogen absorbed. In conditions of constant pressure p , the dependence of the rate constant k from temperature is described by means of the Arrhenius equation:

$$k(T)|_p = A \cdot e^{-\frac{E_a}{R \cdot T}} \quad (4)$$

where E_a is, again, the activation energy and A represents the pre-exponential factor. As a first step, it is necessary to identify the model $f(\alpha)$ that best represents the intrinsic reaction mechanism for Equation (3). Then, the rate constant k can be calculated by expressing Equation (3) as the integral of $d\alpha$ after $f(\alpha)$, i.e., the integral reaction model $g(\alpha)$:

$$g(\alpha) = \int_0^\alpha \frac{d\alpha}{f(\alpha)} = k(T) \cdot t \quad (5)$$

The value of the rate constant can be obtained from the slope of the best model linear fitting, plotting the integral reaction model against time [32]. In this study, the fitting has been performed in a transformed fraction range between 0.10 and 0.95. Moreover, the calculation has been performed only for the absorption process at 30 bar of H_2 (Figure 3a). Taking into account $g(\alpha)$, the best fit was obtained with the Johnson-Mehl-Avrami model with one-dimensional interface-controlled reaction

(JMA, $n = 1$), in agreement with reported works [24,29,33]. After the determination of the rate constants for several temperatures, the activation energy value can be calculated from the slope in the graph of $\ln(k)$ against $1000/T$, as shown in Figure 3b.

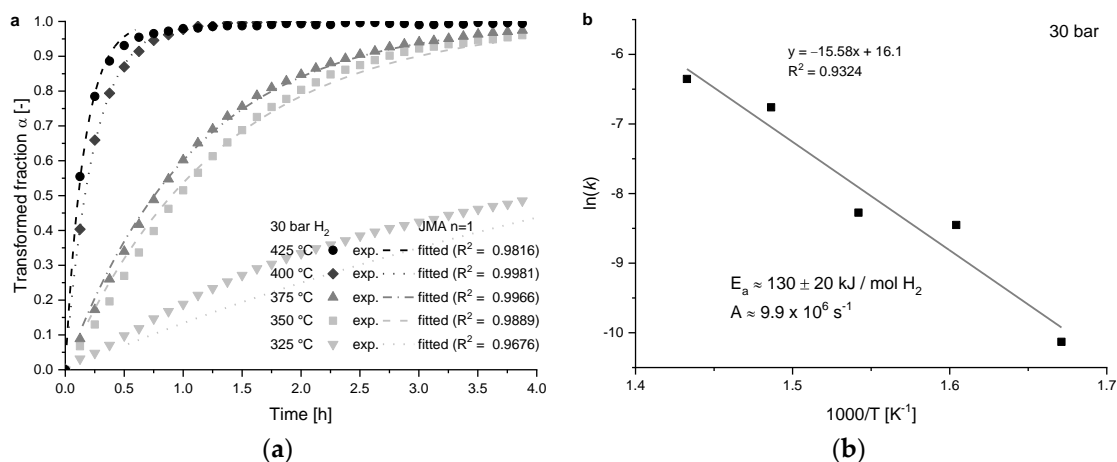


Figure 3. (a) Transformed fraction α plotted vs time under 30 bar of H_2 at different temperatures with the relative fits by JMA $n = 1$ model; (b) The corresponding calculation of the activation energy value, applying Arrhenius equation.

In agreement with Equation (4), the slope of the segment fitting the data linearly corresponds to the activation energy value divided by the ideal gas constant R . Thus, following this method for the case of 30 bar of H_2 pressure, the value of the activation energy is $130 \pm 20 \text{ kJ mol}^{-1} H_2$. This value and the one obtained applying the Kissinger method present a difference, which is discussed in further detail in Section 4.1.

3.1.2. Cycling Behaviour

The reversible hydrogen capacity and its corresponding kinetic behaviour, both for the hydrogenation and dehydrogenation processes, are analysed in this section. In Figure 4a, the reversible hydrogen capacity (obtained from desorption data) is displayed as a function of 20 cycles for 150 mg of compacted and uncompact material. Additionally, the hydrogen capacity for a 500 mg sample is shown and compared. In Figure 4b, its kinetic behaviour is described by plotting the time required to complete 80% of the reaction upon cycling; in these experiments, the absorption has been performed under 50 bar H_2 at 350 °C, and the desorption under 2 bar H_2 at 400 °C.

Not including the first three cycles of the pelletised sample, one can observe how the values are, on average, decreasing with a linear trend. In comparison with the 150 mg loose powder sample, this trend is lower for the compacted sample by a factor of about 2.5, and even by a factor close to 8.5 with the 500 mg pellet. The variation from the average value is almost comparable in all the three different samples considered. It is important to mention that the observed capacity oscillations during cycling are related to the experimental error of the volumetric technique. The reason behind the marked capacity increase for the first three cycles of the compacted sample has been already discussed in a previous publication [25]. It is assumed that the lower absorption in the first tests and the improving performance with cycling can be ascribed to two different reasons. First, as the hydrogen content increases, the necessary expansion of the material is hindered, to a certain extent, by the compaction of the material itself. Second, hydrogen can hardly access the core of the compact pellet due to a dense shell of hydride phase, which is formed on the outer part of the pellet.

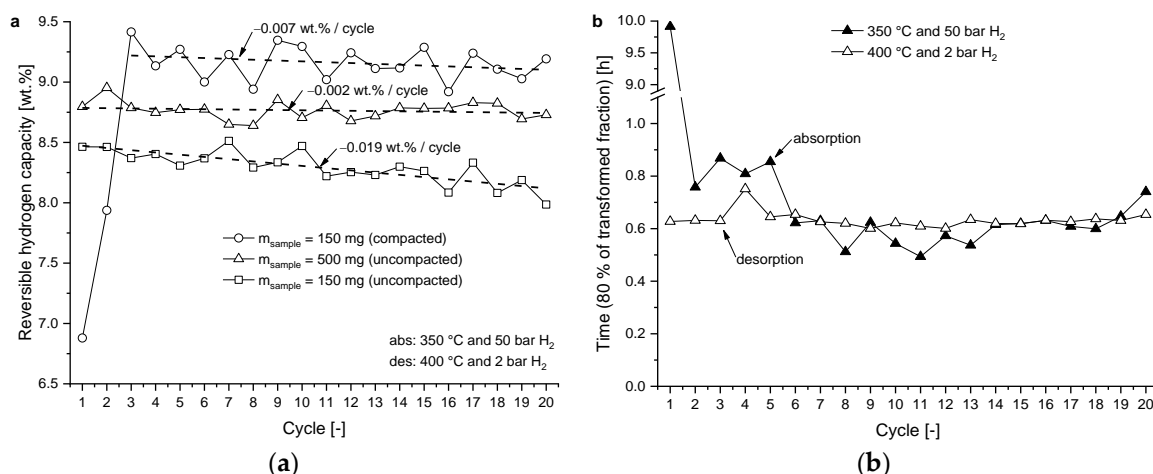


Figure 4. (a) Quantity of hydrogen desorbed at 400 °C and 2 bar H_2 upon cycling, for different amounts of compacted/uncompacted samples after absorption at 350 °C and 50 bar H_2 ; (b) Time for absorption and desorption of 80% transformed fraction upon cycling for the 500 mg sample.

According to the values of the hydrogen quantities over cycling, displayed in Figure 4a, the sample in compacted form is the one with the highest capacity, with an average value of 9.2 wt %, followed by the uncompacted 500 mg samples with a value of 8.8 wt %, and then from 150 mg with a value of 8.3 wt %. A clear and fast degradation of the performance can be observed only for the 150 mg loose powder sample. It is noticeable that the hydrogen quantity of 13.04 wt %, calculated from the desorbed state (Equation (1)), is not reached; the reason for this will be discussed later in Section 4.2.

In Figure 4b, the changes in the kinetic behaviour of the same 500 mg samples shown in Figure 4a have been examined over cycling. The time needed to reach 80% of the transformed fraction in relation to the cycle number is displayed for both the absorption and desorption processes. The first absorption has been already described, being sluggish in many other works, and has been attributed to a sort of stabilisation process (e.g., [34,35]). After some repetitions, the kinetics for absorption reaches approximately the same value as for desorption. The kinetic behaviour for the hydrogen desorption is nearly constant over cycling (Figure 4b).

4. Discussion

4.1. Kinetic Behaviour

As reported previously in Section 3.1.1., the activation energy values have been estimated with the DSC technique for desorption at 3 bar (350 ± 20 kJ mol⁻¹ H_2 and 238 ± 4 kJ mol⁻¹ H_2 for the dehydrogenation of MgH_2 and $LiBH_4$, respectively) and absorption at 30 bar (160 ± 20 kJ mol⁻¹ H_2) and 50 bar of H_2 (104 ± 2 kJ mol⁻¹ H_2). The value for absorption under 30 bar H_2 is also calculated by means of the rate constant determination technique (130 ± 20 kJ mol⁻¹ H_2) for comparison. Despite the fact that the error band of the two different methods at 30 bar is quite large, and consequently, the values are overlapping to a certain extent, the determination by rate constant can be further improved. The values calculated at different hydrogen pressures suggest that the pressure influences the activation energy. Under higher H_2 pressure, the absorption activation energy is remarkably lowered. The Arrhenius equation does not reflect this connection. Even though the experiments to determine the rate constants have been executed under constant set pressure, the equilibrium pressure varies, owing to its correlation with the temperature; thus, the driving force also changes at different temperatures.

According to the work of Rudman [36], the equation previously applied for the rate constant (Equation (4)) needs to be extended with a term considering the driving force $f(p, p_{eq})$:

$$k(p, T) = \left(A \cdot e^{-\frac{E_a}{RT}} \right) \cdot f(p, p_{eq}) \quad (6)$$

This added term reflects the correlation between the set pressure p and the equivalent equilibrium pressure p_{eq} at the desired temperature T . The equilibrium pressure is determined by the van't Hoff equation [3], and thus, the driving force term becomes also a function of the temperature. For this driving force term, several functions have been suggested. The one that best describes the pressure dependence is shown in Equation (7):

$$f(p, p_{eq}) = \ln\left(\frac{p}{p_{eq}}\right) \quad (7)$$

The logarithm of the ratio between the pressure p and the equilibrium pressure p_{eq} represents the free energy change in the sorption process [37]. This is one of the most commonly used pressure dependencies in the literature (e.g., [37,38]). It assumes that the rate-limiting step is associated with chemical reaction in the interface. This is in agreement with the fitted JMA model with $n = 1$ (Figure 3), indicating a one-dimensional interface-controlled mechanism during hydrogenation. For the equilibrium pressure, the values of enthalpy and entropy obtained experimentally by Vajo et al. [21] have been inserted in the calculations. Applying the approach described in the paragraph above, the activation energy value thus calculated increases to $160 \pm 20 \text{ kJ mol}^{-1} \text{ H}_2$, and the goodness of fit reaches 0.964; this is a significant improvement if compared with the calculation performed without the driving force term (Figure 5).

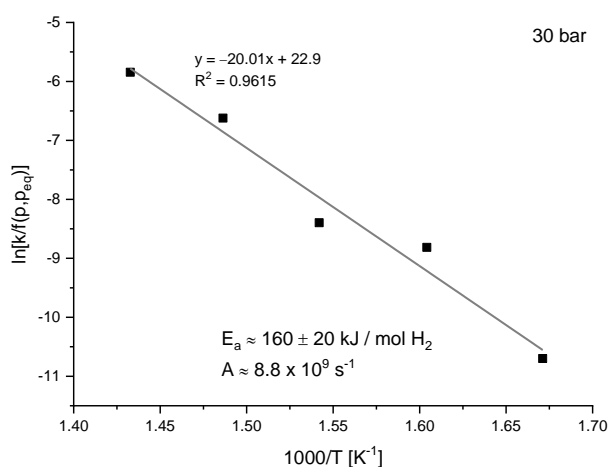


Figure 5. Plot of the data for calculating the activation energy value for absorption at 30 bar, according to the modified Arrhenius equation, extended with the driving force term.

This value is in perfect agreement with the one obtained applying the DSC method ($160 \pm 20 \text{ kJ mol}^{-1} \text{ H}_2$). The higher pressure leads to faster kinetic behaviour, since a larger driving force speeds up the rate-limiting step. Hence, the difference between the values obtained at 30 bar and 50 bar of H_2 can be easily explained.

The value for the first desorption step amounts to $350 \pm 20 \text{ kJ mol}^{-1} \text{ H}_2$ (Figure 2b). In literature, activation energy values for the decomposition of pure MgH_2 are reported in the range of 160 to 206 $\text{kJ mol}^{-1} \text{ H}_2$ [10,11,39]. For transition metals and MgH_2 doped with transition metal compounds, the activation energy values are lowered to about 60 to 120 $\text{kJ mol}^{-1} \text{ H}_2$ depending on the additive molar content [12,13,40–42]. The rate-limiting step for the decomposition of MgH_2 is generally

an interface-controlled movement. However, the value obtained here is higher than that for this process [8,9].

The value for the second desorption step amounts to $238 \pm 4 \text{ kJ mol}^{-1} \text{ H}_2$ (Figure 2b), and is in good agreement with the value calculated by Puszkiel et al. [33]. Based on the Prout–Tompkins autocatalytic model [43], it has been proposed that the second step of the reaction is related to the improved nucleation and growth of the MgB_2 species promoted by the initial formation of MgB_2 nuclei.

In summary, the results and analyses show that TiCl_3 is an additive much more effective in improving the absorption kinetic behaviour, rather than the desorption one (for the Li-RHC system [24]), considering the diverse rate-limiting steps as already indicated in a previous study [16].

4.2. Reversible Hydrogen Capacity

In the following lines, the discussion is focused on the reversible hydrogen capacity. The maximum theoretical gravimetric density of the material of 11.54 wt % has not been reached in this study after several cycles (see Section 3.1.2.). In fact, this capacity is already slightly reduced by the addition of the 0.05 mol of TiCl_3 . Figure 6 shows the XRD analyses of the material after milling and cycling. After milling, the XRD pattern exhibits reflections mainly coming from MgB_2 , LiH, and LiCl. There is just one reflection at around $2\theta = 36^\circ$ that might belong to free Mg, though it is not clear. In the case of the material after cycling and in dehydrogenated state, the presence of MgB_2 , LiH, LiCl, and free Mg is noticed. It is important to point out that TiCl_3 is not detected after milling and cycling. The presence of LiCl suggests that TiCl_3 interacts with the major phases, i.e., $2\text{LiH} + \text{MgB}_2$.

In order to investigate the interactions between TiCl_3 and $2\text{LiH} + \text{MgB}_2$, phase equilibrium compositions calculations have been carried out with the software HSC chemistry [26]. In the calculations conditions are considered, such as mechanical milling (MM), first hydrogenation, and first dehydrogenation, for the $2\text{LiH} + \text{MgB}_2 + 0.05\text{TiCl}_3$ material.

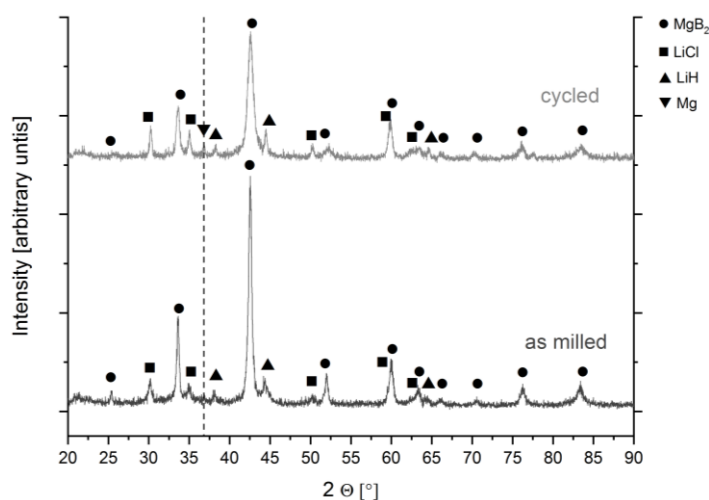
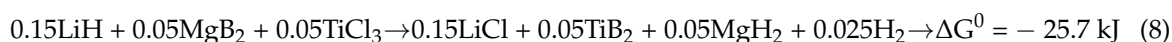


Figure 6. XRD patterns of the sample after milling (as milled) and after the second hydrogenation and dehydrogenation (cycled).

The results obtained from the phase composition equilibrium calculation can be seen in Table 1. The equilibrium calculations predict that after milling, the formation of LiCl, TiB_2 , MgH_2 , and release of H_2 , are thermodynamically favored, according to reaction (8). After the first hydrogenation and dehydrogenation, the calculations suggest that TiB_2 and LiCl remain stable (Table 1).



The addition of transition metal halides to the Li-RHC has already been described as responsible for the formation of nanosized transition metal borides and LiX (X = halide) as byproducts [29,35]. In the literature, the formation of volatile Ti(BH₄)₃ from the interaction between LiBH₄ and Ti halides has been also proposed [44,45]. However, it has been already reported that the presence of H₂ overpressure suppresses the further formation of volatile species [46–48]. Moreover, Kang et al. and Karimi et al. have found that the interaction between titanium fluorides (TiF₃ and TiF₄) and Li-RHC promotes the formation of nanosized TiB₂ during milling [49,50]. Moreover, the release of H₂ during the processing in the planetary mill has already been verified for several other complex hydrides [50,51].

Therefore, the thermodynamic equilibrium calculations and reported works suggest that during the milling process, and subsequent hydrogen interaction, the formation of highly dispersed nanosized TiB₂ occurs. The short-range order TiB₂ cannot be detected by XRD analyses, in agreement with Figure 6. These nanosized boride species act as nucleation sites for MgB₂ upon desorption, accelerating its growth and leading to a further crystallite refinement [29,35]. Based on reaction (8), it is possible to attribute the observed loss of capacity to the formation of TiB₂ and LiCl, according to reaction (9).

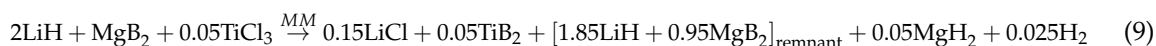
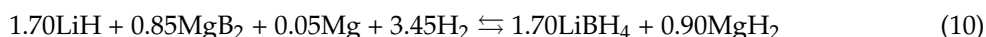


Table 1. Phase equilibrium compositions (mol %) for 2LiH+MgB₂+0.05TiCl₃. Conditions: 25 °C under 1 bar of Ar for MM, 350 °C under 50 bar of H₂ for hydrogenation, and 400 °C under 2 bar of H₂ for dehydrogenation (same conditions used for the cycling in Figure 4).

Species	Starting Composition	After Milling (Milling at 25 °C and 1 bar Ar)	Hydrogenation at 350 °C and 50 bar of H ₂	Dehydrogenation at 400 °C and 2 bar of H ₂
2LiH+MgB ₂ +0.05TiCl ₃				
LiH (s)	66	60	-	55
MgB ₂ (s)	32	30	-	37
TiCl ₃ (s)	2	-	-	-
LiBH ₄ (s)	-	-	62	-
MgH ₂ (s)	-	2	31	-
TiB ₂ (s)	-	2	2	2
Ti (s)	-	-	-	-
TiH ₂ (s)	-	-	-	-
B (s)	-	-	-	-
LiCl (s)	-	5	5	5
Mg (s)	-	-	-	1
B ₂ H ₆ (g)	-	-	-	-
HCl (g)	-	-	-	-
H ₂ (g)	-	1	-	-

For the material in dehydrogenated state, the calculations indicate that the reaction evolves toward the formation of MgB₂, LiH, and small amounts of free Mg, along with the stable TiB₂ and LiCl phases. This is in agreement with the XRD pattern after cycling, shown in Figure 6. Therefore, it is possible to propose the following reaction (10) for the hydrogenation and dehydrogenation of the material upon cycling:



Considering the quantity of hydrogen in reaction (10), and the masses of the solid species in the right side of reaction 9 (so, excluding the released hydrogen), a quantity of about 10 wt % can be absorbed and desorbed, theoretically. The maximum reversible capacity reached in this paper, shown in Figure 4a, is 9.4 wt % at the third cycle for the compacted 150 mg sample. The initial experimental hydrogen capacity (9.4 wt %) is in the range of the calculated value (10 wt %), considering the experimental error band. Hence, the initial loss of hydrogen capacity in comparison with the theoretical one (13.04 wt %, calculated from the desorbed state) is due to the formation of stable species,

such as TiB_2 and LiCl , during the milling process. Moreover, it is possible to observe that the hydrogen capacity is additionally reduced upon cycling, and an average linear fitting denotes a decreasing trend (Figure 4). This decreasing trend in the hydrogen capacity is more noticeable for a small amount of uncompacted material, and less prominent for a higher amount of material (500 mg) or for the same amount of compacted material. The reason behind this declining trend in the hydrogen capacity during cycling can be attributed to the sluggish kinetic behaviour and lack of contact; the latter is likely to be caused by phase separation. The compaction and the mechanical restricted mobility and closeness of the reactants can partially avoid the long-range phase separation [25]. Additionally, larger bed sizes might partially avoid the long-range phase separation. Due to higher temperatures during the reaction, caused by the accumulation of heat, a greater mobility of the reactants inside the bed can develop. Furthermore, for the same reason, higher rates of reaction are possible. However, these higher temperatures can also have a detrimental effect, and lead to slower reaction rates, due to a driving force reduction approaching the equilibrium pressure. Thus, thermal properties, as reported and discussed in the previous publication [16], become highly relevant for larger bed sizes. Another way to avoid long-range phase separation has been shown in the literature by the implementation of graphene-wrapped nanostructures [52–54].

For the kinetic behaviour occurring upon cycling, a clear effect can be observed only on the absorption reaction, and not for desorption. The improvement with a higher number of cycles can be motivated by the enhanced diffusion of hydrogen into the material at high pressure, owing to cracks and pores that might have been forming while absorbing. These defects have been noted on materials that have been compacted before [25]. Of course, this applies, in particular, for the part of the reacting material that remains solid during the sorption reaction (LiH , MgB_2 , and MgH_2).

5. Conclusions

The activation energy values during absorption have been determined as $104 \pm 2 \text{ kJ mol}^{-1} \text{ H}_2$ at 50 bar of H_2 , and $160 \pm 20 \text{ kJ mol}^{-1} \text{ H}_2$ at 30 bar, applying the Kissinger method to several HP-DSC measurements. The second value at 30 bar H_2 is in good agreement with $160 \pm 20 \text{ kJ mol}^{-1} \text{ H}_2$, as calculated by the rate constant, taking into account the effect of the driving force. For the desorption, occurring in two steps, the activation energy values obtained from the measurements with HP-DSC are $350 \pm 20 \text{ kJ mol}^{-1} \text{ H}_2$ and $238 \pm 4 \text{ kJ mol}^{-1} \text{ H}_2$, for the dehydrogenation of MgH_2 and LiBH_4 , respectively. The results and analyses show that the addition of TiCl_3 has an improvement effect on the absorption kinetic behaviour of the Li-RHC system, but does not affect desorption. Again, this proves that separate rate-limiting steps affect the absorption and the desorption reactions, as has already been discussed in the previous study based on thermodynamic properties [16].

Phase equilibrium calculations and experimental evidence suggest that the interaction between the major phases of the material ($2\text{LiH}+\text{MgB}_2$) and the additive (TiCl_3) during milling leads to the formation of TiB_2 and LiCl . This species remains stable upon cycling. The presence of such a stable species results in a theoretical maximum hydrogen capacity of 10 wt %. As a transition metal boride, TiB_2 enhances the kinetic behaviour of the Li-RHC, acting as a nucleation agent for the fast formation of MgB_2 . The mean experimental hydrogen capacity obtained upon 20 hydrogenation /dehydrogenation cycles in these experiments is, at maximum, 9.2 wt % for a pelletised sample. This value stays nearly constant for over 20 absorption/desorption cycles with a slightly decreasing trend ($-0.007 \text{ wt \% per cycle}$). For loose powder material, the mean capacity is lower (8.3 wt %), and the decreasing trend is more notable ($-0.019 \text{ wt \% per cycle}$). The reasons behind the further hydrogen capacity reduction, mainly for the loose powder upon cycling in comparison with the calculated maximum of 10 wt %, taking into account the formation of stable species during milling, were discussed. This fact can be ascribed to slower kinetic behaviour and/or lack of contact between the reactants, probably due to phase separation. Local constraining of the reactants by means of compaction suppresses, at least partially, long-range phase separation.

The results of both studies of the thermodynamic, heat transfer, and kinetic properties will be implemented in future finite elements method (FEM) simulations that will give important insights about the temperature distribution and loading/unloading times for a scaled-up system. This provides the basis for methodical optimization of hydrogen storage systems based on metal hydrides in larger scale.

Author Contributions: J.J. and C.M. conceived and designed the experiments; B.S., A.G., G.A.L. and J.M.B.v.C. supported by analyzing the data; A.M., S.K., M.D. and T.K. contributed by discussing the results; J.J., J.P. and G.C. wrote the paper.

Acknowledgments: The authors are grateful for the partial financial support of the DAAD (German Academic Exchange Service) in the framework of the “VIGONI” Project and in cooperation with the Ministerio de Educación de la Nación Argentina in the frame of the Sandwich Grant Program “ALEARG” (Grant number A/09/75212), CONICET (Consejo Nacional de Investigaciones Científicas y Técnicas) as well as the COST Action MP1103 (“Nanostructured materials for solid-state hydrogen storage”).

Conflicts of Interest: The authors declare no conflict of interest.

Nomenclature

Symbol	Description
A	Arrhenius factor
E_a	Activation energy
f	Function
$g(\alpha)$	Reaction model function
k	Rate constant
p	Pressure
R	Gas constant
t	Time
T	Temperature
α	Transformed fraction
β	Heating rate

References

- Schlapbach, L.; Züttel, A. Hydrogen-storage materials for mobile applications. *Nature* **2001**, *414*, 353–358. [[CrossRef](#)] [[PubMed](#)]
- Lide, D.R. *Handbook of Chemistry and Physics*; CRC Press: London, UK, 1994.
- Varin, R.A.; Czujko, T.; Wronski, Z.S. *Nanomaterials for Solid State Hydrogen Storage*; Springer: New York, NY, USA, 2009.
- Jepsen, J.; Bellosta von Colbe, J.M.; Klassen, T.; Dornheim, M. Economic potential of complex hydrides compared to conventional hydrogen storage systems. *Int. J. Hydrogen Energy* **2012**, *37*, 4204–4214. [[CrossRef](#)]
- Schlesinger, H.I.; Brown, H.C. Metallo Borohydrides. III. Lithium Borohydride. *J. Am. Chem. Soc.* **1940**, *62*, 3429–3435. [[CrossRef](#)]
- Varin, R.A.; Li, S.; Wronski, Z.; Morozova, O.; Khomenko, T. The effect of sequential and continuous high-energy impact mode on the mechano-chemical synthesis of nanostructured complex hydride Mg_2FeH_6 . *J. Alloys Compd.* **2005**, *390*, 282–296. [[CrossRef](#)]
- Sakintuna, B.; Lamari-Darkrim, F.; Hirscher, M. Metal hydride materials for solid hydrogen storage: A review. *Int. J. Hydrogen Energy* **2007**, *32*, 1121–1140. [[CrossRef](#)]
- Martin, M.; Gommel, C.; Borkhart, C.; Fromm, E. Absorption and desorption kinetics of hydrogen storage alloys. *J. Alloys Compd.* **1996**, *238*, 193–201. [[CrossRef](#)]
- Konstanchuk, Y.G.; Ivanov, E.; Boldyrev, V. Interaction of alloys and intermetallic compounds obtained by mechanochemical methods with hydrogen. *Russ. Chem. Rev.* **1998**, *67*, 69–79. [[CrossRef](#)]
- Fernández, J.F.; Sánchez, C.R. Rate determining step in the absorption and desorption of hydrogen by magnesium. *J. Alloys Compd.* **2002**, *340*, 189–198. [[CrossRef](#)]

11. Puzskiel, J.A. *Preparation, Study and Optimization of Complex Hydrides for Hydrogen Storage*; Universidad Nacional de Cuyo: Ciudad de Mendoza, Argentina, 2012.
12. Hanada, N.; Ichikawa, T.; Fujii, H. Catalytic Effect of Nanoparticle 3d-Transition Metals on Hydrogen Storage Properties in Magnesium Hydride MgH₂ Prepared by Mechanical Milling. *J. Phys. Chem. B* **2005**, *109*, 7188–7194. [[CrossRef](#)] [[PubMed](#)]
13. Liang, G.; Huot, J.; Boily, S.; Van Neste, A.; Schulz, R. Catalytic effect of transition metals on hydrogen sorption in nanocrystalline ball milled MgH₂-Tm (Tm=Ti, V, Mn, Fe and Ni) systems. *J. Alloys Compd.* **1999**, *292*, 247–252. [[CrossRef](#)]
14. Suryanarayana, C. Mechanical alloying and milling. *Prog. Mater. Sci.* **2001**, *46*, 1–184. [[CrossRef](#)]
15. Huot, J.; Ravnsbæk, D.B.; Zhang, J.; Cuevas, F.; Latroche, M.; Jensen, T.R. Mechanochemical synthesis of hydrogen storage materials. *Prog. Mater. Sci.* **2013**, *58*, 30–75. [[CrossRef](#)]
16. Jepsen, J.; Milanese, C.; Puzskiel, J.; Girella, A.; Schiavo, B.; Lozano, G.A.; Capurso, G.; Colbe, J.M.B.; Marini, A.; Kabelac, S.; et al. Fundamental material properties of the 2LiBH₄-MgH₂ reactive hydride composite for hydrogen storage (I) Thermodynamic and heat transfer properties. *Energies* **2018**, *11*, 1081. [[CrossRef](#)]
17. Bogdanović, B.; Bohmhammel, K.; Christ, B.; Reiser, A.; Schlichte, K.; Vehlen, R.; Wolf, U. Thermodynamic investigation of the magnesium-hydrogen system. *J. Alloys Compd.* **1999**, *282*, 84–92. [[CrossRef](#)]
18. Dornheim, M.; Doppiu, S.; Barkhordarian, G.; Boesenberg, U.; Klassen, T.; Gutfleisch, O.; Bormann, R. Hydrogen storage in magnesium-based hydrides and hydride composites. *Scr. Mater.* **2007**, *56*, 841–846. [[CrossRef](#)]
19. Westerwaal, R.J.; Haije, W.G. *Evaluation Solid-State Hydrogen Storage Systems*; ECN Publication: Petten, The Netherlands, 2008.
20. Barkhordarian, G.; Klassen, T.; Dornheim, M.; Bormann, R. Unexpected kinetic effect of MgB₂ in reactive hydride composites containing complex borohydrides. *J. Alloys Compd.* **2007**, *440*, L18–L21. [[CrossRef](#)]
21. Vajo, J.J.; Skeith, S.L.; Mertens, F. Reversible Storage of Hydrogen in Destabilized LiBH₄. *J. Phys. Chem. B* **2005**, *109*, 3719–3722. [[CrossRef](#)] [[PubMed](#)]
22. Züttel, A.; Wenger, P.; Rentsch, S.; Sudan, P.; Mauron, P.; Emmenegger, C. LiBH₄ a new hydrogen storage material. *J. Power Sources* **2003**, *118*, 1–7. [[CrossRef](#)]
23. Puzskiel, J.; Garroni, S.; Milanese, C.; Gennari, F.; Klassen, T.; Dornheim, M.; Pistidda, C. Tetrahydroborates: Development and Potential as Hydrogen Storage Medium. *Inorganics* **2017**, *5*, 74. [[CrossRef](#)]
24. Jepsen, J. *Technical and Economic Evaluation of Hydrogen Storage Systems Based on Light Metal Hydrides*; HZG Report 2014-2; Helmut-Schmidt-University: Hamburg, Germany, 2014.
25. Jepsen, J.; Milanese, C.; Girella, A.; Lozano, G.A.; Pistidda, C.; Bellosta von Colbe, J.M.; Marini, A.; Klassen, T.; Dornheim, M. Compaction pressure influence on material properties and sorption behaviour of LiBH₄-MgH₂ composite. *Int. J. Hydrogen Energy* **2013**, *38*, 8357–8366. [[CrossRef](#)]
26. *HSC Chemistry*, version 9.4.1; Software for Various Kinds of Chemical Reactions and Equilibria Calculations; Outotec: Espoo, Finland, 2018.
27. Kissinger, H.E. Reaction Kinetics in Differential Thermal Analysis. *Anal. Chem.* **1957**, *29*, 1702–1706. [[CrossRef](#)]
28. Bösenberg, U.; Doppiu, S.; Mosegaard, L.; Barkhordarian, G.; Eigen, N.; Borgschulte, A.; Jensen, T.R.; Cerenius, Y.; Gutfleisch, O.; Klassen, T.; et al. Hydrogen sorption properties of MgH₂-LiBH₄ composites. *Acta Mater.* **2007**, *55*, 3951–3958. [[CrossRef](#)]
29. Bösenberg, U.; Kim, J.W.; Gossler, D.; Eigen, N.; Jensen, T.R.; von Colbe, J.M.B.; Zhou, Y.; Dahms, M.; Kim, D.H.; Günther, R.; et al. Role of additives in LiBH₄-MgH₂ reactive hydride composites for sorption kinetics. *Acta Mater.* **2010**, *58*, 3381–3389. [[CrossRef](#)]
30. Fedneva, E.M.; Alpatova, V.L.; Mikheeva, V.I. Thermal stability of lithium tetrahydroborate. *Russ. J. Inorg. Chem.* **1964**, *9*, 826–827.
31. Nakagawa, T.; Ichikawa, T.; Hanada, N.; Kojima, Y.; Fujii, H. Thermal analysis on the Li-Mg-B-H systems. *J. Alloys Compd.* **2007**, *446* (Suppl. C), 306–309. [[CrossRef](#)]
32. Khawam, A.; Flanagan, D.R. Solid-state kinetic models: Basics and mathematical fundamentals. *J. Phys. Chem. B* **2006**, *110*, 17315–17328. [[CrossRef](#)] [[PubMed](#)]
33. Puzskiel, J.A.; Castro Riglos, M.V.; Ramallo-Lopez, J.M.; Mizrahi, M.; Karimi, F.; Santoru, A.; Hoell, A.; Gennari, F.C.; Larochette, P.A.; Pistidda, C.; et al. A novel catalytic route for hydrogenation-dehydrogenation

- of $2\text{LiH} + \text{MgB}_2$ via in situ formed core-shell Li_xTiO_2 nanoparticles. *J. Mater. Chem. A* **2017**, *5*, 12922–12933. [[CrossRef](#)]
34. Pinkerton, F.E.; Meyer, M.S.; Meisner, G.P.; Balogh, M.P.; Vajo, J.J. Phase Boundaries and Reversibility of $\text{LiBH}_4/\text{MgH}_2$ Hydrogen Storage Material. *J. Phys. Chem. C* **2007**, *111*, 12881–12885. [[CrossRef](#)]
 35. Bösenberg, U. *$\text{LiBH}_4\text{-MgH}_2$ Composites for Hydrogen Storage*; Technische Universität Hamburg-Harburg: Hamburg, Germany, 2009.
 36. Rudman, P.S. Hydriding and dehydriding kinetics. *J. Less Common Metals* **1983**, *89*, 93–110. [[CrossRef](#)]
 37. Lozano, G.A.; Ranong, C.N.; Bellosta von Colbe, J.M.; Bormann, R.; Fieg, G.; Hapke, J.; Dornheim, M. Empirical kinetic model of sodium alanate reacting system (I). Hydrogen absorption. *Int. J. Hydrogen Energy* **2010**, *35*, 6763–6772. [[CrossRef](#)]
 38. Marty, P.; Fourmigue, J.F.; Rango, P.D.; Fruchart, D.; Charbonnier, J. Numerical simulation of heat and mass transfer during the absorption of hydrogen in a magnesium hydride. *Energy Convers. Manag.* **2006**, *47*, 3632–3643. [[CrossRef](#)]
 39. Patah, A.; Takasaki, A.; Szmyd, J.S. Influence of multiple oxide ($\text{Cr}_2\text{O}_3/\text{Nb}_2\text{O}_5$) addition on the sorption kinetics of MgH_2 . *Int. J. Hydrogen Energy* **2009**, *34*, 3032–3037. [[CrossRef](#)]
 40. Barkhordarian, G.; Klassen, T.; Bormann, R. Kinetic investigation of the effect of milling time on the hydrogen sorption reaction of magnesium catalyzed with different Nb_2O_5 contents. *J. Alloys Compd.* **2006**, *407*, 249–255. [[CrossRef](#)]
 41. Milanese, C.; Girella, A.; Garroni, S.; Bruni, G.; Berbeni, V.; Matteazzi, P.; Marini, A. Synergetic effect of C (graphite) and Nb_2O_5 on the H_2 sorption properties of the Mg-MgH_2 system. *Int. J. Hydrogen Energy* **2010**, *35*, 9027–9037. [[CrossRef](#)]
 42. Pighin, S.A.; Capurso, G.; Lo Russo, S.; Peretti, H.A. Hydrogen sorption kinetics of magnesium hydride enhanced by the addition of $\text{Zr}_8\text{Ni}_{21}$ alloy. *J. Alloys Compd.* **2012**, *530*, 111–115. [[CrossRef](#)]
 43. Brown, M.E. The Prout-Tompkins rate equation in solid-state kinetics. *Thermochim. Acta* **1997**, *300*, 93–106. [[CrossRef](#)]
 44. Fang, Z.Z.; Ma, L.P.; Kang, X.D.; Wang, P.J.; Wang, P.; Cheng, H.M. In situ formation and rapid decomposition of $\text{Ti}(\text{BH}_4)_3$ by mechanical milling LiBH_4 with TiF_3 . *Appl. Phys. Lett.* **2009**, *94*, 044104. [[CrossRef](#)]
 45. Callini, E.; Szilagyi, P.A.; Paskevicius, M.; Stadie, N.P.; Rehault, J.; Buckley, C.E.; Borgschulze, A.; Zuttel, A. Stabilization of volatile $\text{Ti}(\text{BH}_4)_3$ by nano-confinement in a metal-organic framework. *Chem. Sci.* **2016**, *7*, 666–672. [[CrossRef](#)] [[PubMed](#)]
 46. Kim, K.-B.; Shim, J.-H.; Cho, Y.W.; Oh, K.H. Pressure-enhanced dehydrogenation reaction of the $\text{LiBH}_4\text{-YH}_3$ composite. *Chem. Commun.* **2011**, *47*, 9831–9833. [[CrossRef](#)] [[PubMed](#)]
 47. Kim, K.-B.; Shim, J.-H.; Park, S.-H.; Choi, I.-S.; Oh, K.H.; Cho, Y.W. Dehydrogenation Reaction Pathway of the $\text{LiBH}_4\text{-MgH}_2$ Composite under Various Pressure Conditions. *J. Phys. Chem. C* **2015**, *119*, 9714–9720. [[CrossRef](#)]
 48. Kim, K.-B.; Shim, J.-H.; Oh, K.H.; Cho, Y.W. Role of Early-Stage Atmosphere in the Dehydrogenation Reaction of the $\text{LiBH}_4\text{-YH}_3$ Composite. *J. Phys. Chem. C* **2013**, *117*, 8028–8031. [[CrossRef](#)]
 49. Kang, X.; Wang, K.; Zhong, Y.; Yang, B.; Wang, P. A novel three-step method for preparation of a TiB_2 -promoted $\text{LiBH}_4\text{-MgH}_2$ composite for reversible hydrogen storage. *Phys. Chem. Chem. Phys.* **2013**, *15*, 2153–2158. [[CrossRef](#)] [[PubMed](#)]
 50. Karimi, F.; Castro Riglos, M.; Santoru, A.; Hoell, A.; Raghuvanshi, V.; Milanese, C.; Bergemann, N.; Pistidda, C.; Nolis, P.; Baró, M.; et al. In situ formation of TiB_2 nanoparticles for enhanced dehydrogenation/hydrogenation reaction kinetics of $\text{LiBH}_4\text{-MgH}_2$ as a reversible solid-state hydrogen storage system. *J. Phys. Chem. C* **2018**. under review, (Manuscript jp-2018-02258a).
 51. Bellosta von Colbe, J.M.; Bogdanovic, B.; Felderhoff, M.; Pommerin, A.; Schüth, F. Recording of hydrogen evolution—A way for controlling the doping process of sodium alanate by ball milling. *J. Alloys Compd.* **2004**, *370*, 104–109. [[CrossRef](#)]
 52. Xia, G.; Tan, Y.; Wu, F.; Fang, F.; Sun, D.; Guo, Z.; Huang, Z.; Yu, X. Graphene-wrapped reversible reaction for advanced hydrogen storage. *Nano Energy* **2016**, *26*, 488–495. [[CrossRef](#)]

53. Xia, G.; Tan, Y.; Chen, X.; Fang, F.; Sun, D.; Li, X.; Guo, Z.; Yu, X. Oxygen-free Layer-by-Layer Assembly of Lithiated Composites on Graphene for Advanced Hydrogen Storage. *Adv. Sci.* **2017**, *4*, 1600257. [[CrossRef](#)] [[PubMed](#)]
54. Xia, G.; Tan, Y.; Chen, X.; Sun, D.; Guo, Z.; Liu, H.; Ouyang, L.; Zhu, M.; Yu, X. Monodisperse Magnesium Hydride Nanoparticles Uniformly Self-Assembled on Graphene. *Adv. Mater.* **2015**, *27*, 5981–5988. [[CrossRef](#)] [[PubMed](#)]



© 2018 by the authors. Licensee MDPI, Basel, Switzerland. This article is an open access article distributed under the terms and conditions of the Creative Commons Attribution (CC BY) license (<http://creativecommons.org/licenses/by/4.0/>).